Journal of Materials Chemistry

Cite this: DOI: 10.1039/c1jm10918a

www.rsc.org/materials

PAPER

Evolution of zinc oxide nanostructures through kinetics control†

Jian Shi,[a] Hao Hong,[b] Yong Ding,[c] Yunan Yang,[b] Fei Wang,[a] Weibo Cai*[b] and Xudong Wang*[a]

Received 2nd March 2011, Accepted 7th April 2011
DOI: 10.1039/c1jm10918a

In-depth understanding of the kinetics of the vapor deposition process is substantial for advancing this capable bottom-up nanostructure synthesis approach into a versatile large-scale nanomanufacturing technology. In this paper, we report a systematic study of the vapor deposition kinetics of ZnO nanomaterials under controlled atmosphere and properly refined deposition conditions. The experiments clearly evidenced the self-catalyzed growth of ZnO NWs *via* the formation of ZnO nanoflowers. This result illustrated how ZnO morphologies were associated with the discrepancy between oxidation rate and condensation rate of Zn. The capability of switching the NW morphologies and possibly mechanisms was demonstrated by kinetically controlling the deposition system. The high Zn composition during the deposition resulted in strongly luminescent NWs, which can be used for optical imaging applications. This research discovered a fundamental kinetics that governs the mechanisms and morphology selection of nanostructures in a non-catalyst growth system.

Introduction

The last two decades have witnessed a rapid development of nanowire (NW) structures and their intriguing applications in electronics, photonics, electromechanics and biotechnology.[1–8] In order to covert the promising NW-based nanoscience and nanotechnology into practical products, the first prerequisite is the capability of synthesizing the NW building blocks with designed dimensions, morphologies, compositions, and reliable functionalities at large scale. Numerous researches are currently allocated on understanding the nanoscale nucleation and growth behavior so as to secure the necessary controllability and repeatability of NW manufacturing.[9–19] Among several well-accepted NW growth strategies, vapor deposition approaches are distinguished by their versatility, high crystal quality products, and potential scalability.[1] Foreign metallic catalysts were widely used to direct the orientation and control the size of NWs *via* a vapor–liquid–solid (VLS) process, which has been intensively studied and well understood.[10,12–15,18] Alternatively, NWs can be synthesized without using any foreign catalysts.[9,11,20–25] It offers a high lattice purity that is beneficial in many realms, such as eliminating unintentional doping and avoiding the poisonous effect of transition metals. It could also create many other morphologies including nanobelts, nanocombs, and even three-dimensional NW networks.[11,23,24,26] Self-catalyzed growth and the vapor–solid (VS) process are the two mechanisms suggested for the formation of nanostructures without foreign catalysts, where an excess of metal adatoms would be responsible for the self-catalyzed growth;[9,26] screw dislocations have been observed to be able to lead NW growth by providing deposition sites for a VS process.[11] Many different evidences have been presented to support the proposed mechanisms and to explain the growth of nanostructures for different material systems and under different experimental conditions.[9,20,22,25] However, the connection between different experimental observations and the two growth mechanisms is still missing, which seriously limits our capability of controlling the morphology and scaling up the synthesis. Thus, in-depth understandings of the kinetics of the vapor deposition process are greatly desired, which is substantial for advancing this powerful bottom-up synthesis approach into a versatile nanomanufacturing technology. In this paper, we report a systematic study of the vapor deposition kinetics of ZnO nanomaterials under controlled atmosphere and properly refined deposition conditions. The experiments clearly evidenced the self-catalyzed growth of ZnO NWs *via* the formation of ZnO NW flowers. This result illustrated how ZnO morphologies were associated with the discrepancy between oxidation rate and condensation rate of Zn. The capability of switching the NW morphologies and possibly mechanisms was demonstrated by kinetically controlling the deposition system. The high Zn composition during the deposition resulted in strongly luminescent NWs, which can be used for optical imaging applications. This research discovered a fundamental kinetics that governs the mechanisms and morphology selection of nanostructures in a non-catalyst growth system.

[a]*Department of Materials Science and Engineering, University of Wisconsin-Madison, USA. E-mail: xudong@engr.wisc.edu; wcai@uwhealth.org*
[b]*Departments of Radiology, Medical Physics, and Biomedical Engineering, University of Wisconsin-Madison, USA*
[c]*School of Materials Science and Engineering, Georgia Institute of Technology, USA*
† Electronic supplementary information (ESI) available. See DOI: 10.1039/c1jm10918a

Experimental section

Growth of ZnO nanostructures

The vapor deposition of ZnO nanostructure was performed in an alumina tube placed inside a temperature-gradient tube furnace. Pure ZnO powder was used as the precursor and located at the center of the tube. Cooling collars are installed on the two ends of the alumina tube to create a dramatic temperature gradient. The tube was filled with argon at a constant flow rate of 50 sccm. The pressure was kept at a very low level (39 Pa) in order to create a high Zn vapor concentration to scrutinize the kinetics of ZnO deposition. Three polycrystalline alumina substrates (15 cm in length and 1 cm in width) were lined together and located 5 cm away from the source, which covered a broad deposition temperature range. The system was heated to 1000 °C during the first 26 minutes, which reached 1400 °C after another 44 minutes. The precursor was found completely vaporized after the temperature reached 1400 °C. Subsequently, the system was cooled down to room temperature naturally under the same argon atmosphere.

Syntheses of NW–PEG and NW–PEG–RGD

Organic carboxylic acids with high stability and high equilibrium binding constants are the most common anchoring groups on surfaces of metal oxides such as TiO_2, SnO_2, and ZnO, mainly through the carboxylate bidentate coordination bonds to one or two metal atoms.[27,28] Modifications of ZnO colloidal nanomaterials with organic carboxylic acids have also been reported.[29] On the basis of these prior results, here we used 3-mercaptopropionic acid to introduce sulfhydryl groups onto the surface of ZnO NWs for further functionalization.

Three milligrams (mg) of 3-mercaptopropionic acid (Sigma-Aldrich, St Louis, MO) was added to a suspension of 5 mg of ZnO nanowires in 2 mL of dichloromethane (DCM). The resulting mixture was stirred at room temperature (RT) for 1 h. After evaporation of the solvent, the white solid was collected and washed with methanol thoroughly for at least three times. Two mg of resulting product (denoted as "NW–SH") was then reacted with 10 mg of maleimide–polyethylene glycol–succinimidyl carboxy methyl ester (Mal–PEG–SCM, Creative PEGWorks, Winston-Salem, NC) for 1 h at RT in 2 mL of phosphate-buffered saline (PBS, pH = 7.4) in the presence of tris (2-carboxyethyl)phosphine hydrochloride (TCEP, a reducing reagent to prevent disulfide formation, Sigma-Aldrich). The product (*i.e.* NW–PEG) was collected by centrifugation at 8000 rpm for five minutes and washed repeatedly with methanol and Millipore-grade water.

To synthesize NW–PEG–RGD (arginine–glycine–aspartic acid), 10 mg of Mal–PEG–SCM was reacted with 1.3 mg of c(RGDyK) in 2 mL of PBS (pH = 8.5) for 4 h at RT. Subsequently, the pH of the reaction mixture was adjusted to 7. Two mg of NW–SH was added and the reaction was allowed to go on for 1 h at RT in the presence of TCEP. The product (*i.e.* NW–PEG–RGD) was collected by centrifugation at 8000 rpm for five minutes and washed repeatedly with methanol and Millipore-grade water. Both NW–PEG and NW–PEG–RGD were re-suspended in PBS (pH = 7.4) to form a stock solution of 2 mg mL^{-1} for further investigation.

The NW functionalization was confirmed by monitoring change of ζ potential after each step. The ζ potential was measured with a Malvern Zeta Sizer Nano (Malvern Instruments, Westborough, MA). Untreated ZnO NWs had a ζ potential of -29.5 ± 1.8 mV; and it changed to -21.2 ± 2.4 mV after –SH coating, then -26.1 ± 3.5 mV after PEG coating, and eventually -9.1 ± 0.9 mV after RGD coating.

Cellular assay of NW–PEG and NW–PEG–RGD

To investigate the cellular imaging characteristics of functionalized ZnO NWs, different concentrations of NW–PEG or NW–PEG–RGD (1–100 μg mL^{-1}) were used for U87MG cell incubation. From this pilot study, 30 μg mL^{-1} of NW–PEG–RGD exhibited a strong fluorescent signal on the cells with no significant toxicity. Thus, the concentration of 30 μg mL^{-1} was chosen for further investigation in this study.

To determine the integrin $\alpha_v\beta_3$-binding affinity/specificity of NW–PEG–RGD, cold acetone-fixed MCF-7 (human breast cancer, integrin $\alpha_v\beta_3$ negative) and U87MG (human glioblastoma, high integrin $\alpha_v\beta_3$ expression) cells were blocked with 0.1% bovine serum albumin (5 min at RT), incubated with 30 μg mL^{-1} of naked NW, NW–PEG, NW–PEG–RGD or NW–PEG–RGD in the presence of 2 μM of c(RGDyK) for 1 h. Subsequently, the cells were washed with cold PBS thoroughly for three times and examined under a Nikon Eclipse Ti-E fluorescent microscope (excitation: 330–380 nm; emission: 420 nm long-pass; magnification: 200×; exposure time: 0.3 s). All fluorescence images were acquired under the same condition and displayed under the same scale. The representative bright field and fluorescence images are shown in Fig. 5.

Results and discussion

Morphology and structure characterization

Our ZnO nanostructures were growth by thermal decomposition of ZnO powder in a tube furnace at 1400 °C. In order to study the ZnO nanostructure growth behavior, the deposition pressure was kept at a very low level (~39 Pa), which ensured a high Zn vapor concentration. A very slow ramping rate was applied so that an abrupt vapor concentration change became possible during the deposition (see Experimental section for details). The as-synthesized ZnO nanostructures were first investigated by scanning electron microscopy (SEM) and a variety of morphologies (NWs, nanocombs, nanoflowers, Zn–ZnO core–shell NWs, and Zn powders) were observed within the deposition temperature range from ~600 °C to ~100 °C. The interesting ZnO nanoflower structure was observed at the deposition temperature zone of ~410 °C, which was between the conventional ZnO nanostructures (NWs and nanocombs) and the Zn rich structures. Therefore, the ZnO nanoflowers were believed to be the key for understanding the growth kinetics and their structure was carefully investigated.

As shown in Fig. 1a, the substrate was covered with a semi-aligned flower-like structure. Each flower either directly grew from underneath alumina substrate or derived from one crystal core (Fig. 1a). As the dominant morphology in this area, the dimension and morphology of each flower is nearly identical. Closer examination showed that each nanoflower was composed

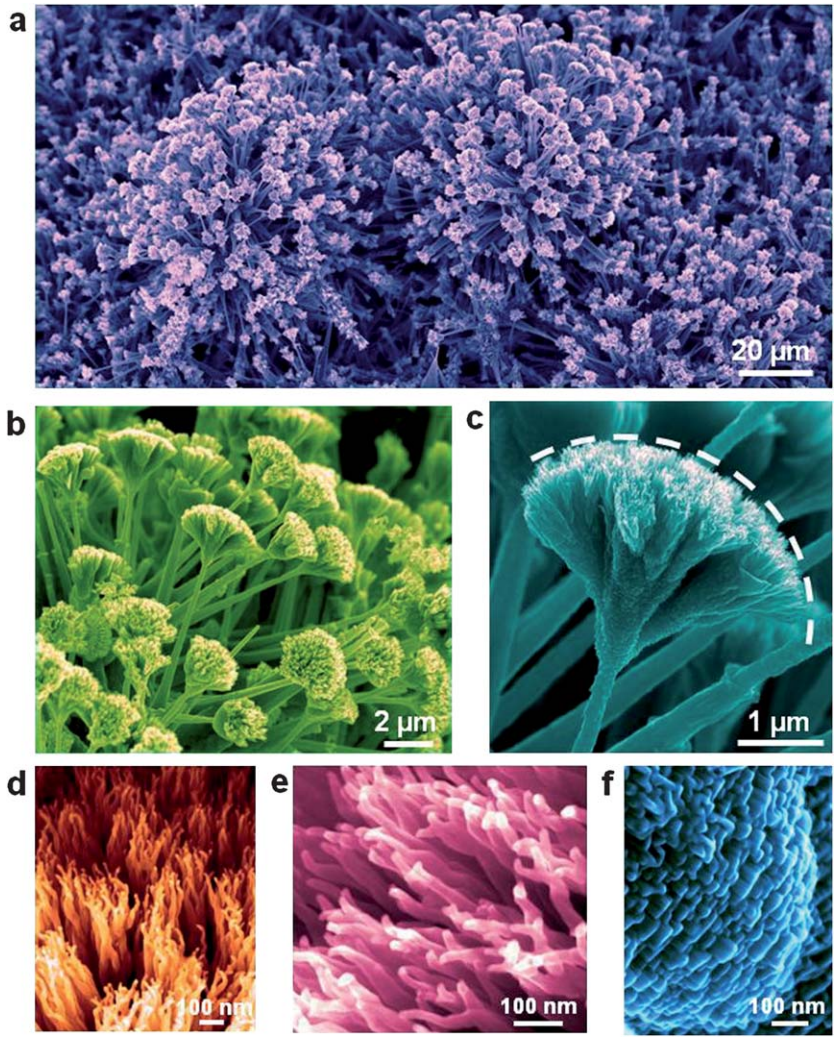

Fig. 1 SEM images of ZnO nanoflower structures. (a) Overview of dense ZnO nanoflowers grown on alumina substrates. (b) A cluster of nanoflowers, where a tapering structure of the nanoflower stems and a spherical growth front of the corollas could be observed. (c) SEM image of a representative nanoflower corolla showing it is constructed by the tiny petals. The sharp interface between the stem and corolla could be clearly distinguished, which implies an abrupt transit of growth behavior. (d) SEM image of the petal arrangement, where a few tens of petals form a cluster and all the clusters make the overall corolla. (e) The top portion of the petals, which have similar dimensions and exhibit a curvy structure. (f) The bottom portion of the petals, which are stacked and fused together, forming a scale-like structure.

of one stem (15–20 μm long) and one corolla (~3 μm in width and ~2 μm in height) (Fig. 1b). The stems exhibited a tapering structure with tips of several hundred nanometres and roots of ~2 μm. It can also be seen that the surface of the stem was rather rough and did not show the regular hexagonal shape (Fig. 1c). At the very end of the stem, a big bundle of small NWs (or petals) assembled into a corolla-like morphology. Closer observation of the corolla structure revealed that a few tens of petals formed one cluster and all of the clusters further integrated into the corolla (Fig. 1d). The top portion of petals was 20–40 nm apart from each other. The observable region of the petals (a few hundred nanometres long) appeared sinuous along the upward direction. Width of the petals was ~20 nm and a small variance of width distribution among these petals could be identified (Fig. 1e). The bottom portion of the petals was stacked and fused together exhibiting a scale-like structure (Fig. 1f). The petal root configuration indicates that each petal was probably evolved from a separated nucleation site on the surface of existing petals.

The crystal structure was further studied using transmission electron microscopy (TEM). The stem with a rough surface is shown in Fig. 2a. Selective area electron diffraction (SAED) revealed that the stem was a single crystal and grew along the [0001] direction. The roughness was resulted from ZnO nanoparticles decorated along the side surfaces. Dark field TEM imaging showed that those nanoparticles did not share the same crystal orientation as the core of the stem (Fig. 2b), which indicates a possible occurrence of a secondary oxidation/deposition process after the growth of stem. Fig. 2c shows the overall structure of a corolla that was broken off from the stem, where the petal assembly can be clearly observed. Interface between the corolla and the stem was characterized by dark field imaging shown in Fig. 2d. Similar to the stem, the main body of the interface showed quality crystalline integrity while the sidewalls were ornamented by scatted ZnO nanoparticles. Further TEM analysis revealed that each petal (the curved small NW) was a single crystal (Fig. 2e). However, they do not have the same

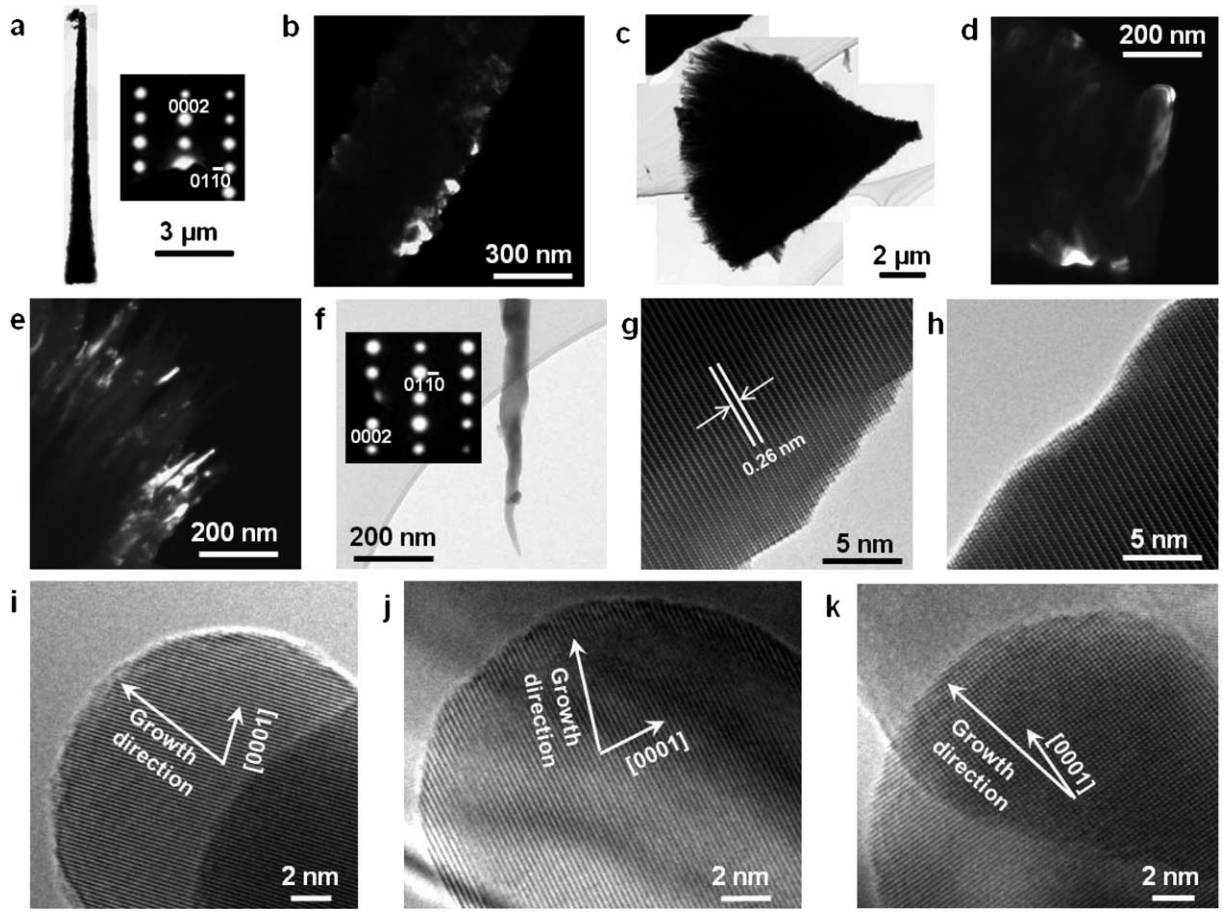

Fig. 2 TEM analyses of the crystal structure of ZnO nanoflowers. (a) TEM image of a typical nanoflower stem showing a tapering structure; inset is the corresponding SAED pattern indicating that the growth is along the [0001] direction. (b) Dark-field TEM image of the stem. The different contrast represents different crystal orientations of the nanoparticles deposited on the surface of the stem. (c) TEM image of an overall corolla structure. (d) Dark-field TEM image of the interface between the corolla and stem, which reveals that the main trunk is single crystalline while the surface is decorated by ZnO nanoparticles. (e) Dark-field TEM image of nanoflower petals showing that each petal is a single crystal. (f) TEM image of an individual petal; inset is the SAED pattern showing that the growth is along the [0001] direction. (g and h) HRTEM images of the petal sidewalls. They demonstrate a wavy shape but no dislocation and amorphous shell was observed. (i–k) HRTEM images of the petal tips that are found to be spherical. The growth directions of the petals are not parallel to the [0001] directions. The spherical shape of the petal tips and their random growth orientations are typical observations.

crystal alignment and orientation, which was evidenced by the different dark field contrasts on different petals.

The petals could come off from the corolla easily during TEM sample preparation, which made the investigation of the single petal structure possible. One single petal is shown in Fig. 2f, where the curvy sidewalls and a tapering trend along the growth direction can be clearly observed. SAED reveals that the petal also grew along the [0001] direction (inset of Fig. 2f). The diameter of the petals varied from tens of nanometres at the root to ~10 nm at the tip. High-resolution TEM (HRTEM) images illustrate that the sidewalls of the petal were composed of high-index facets and no amorphous layer was spotted (Fig. 2g and h). Although surfaces of these petals were rough, no dislocations or stacking faults were observed, thus the overall structure could be considered dislocation-free. The most unconventional structure was found at the petal tip. Unlike typical ZnO NWs which usually exhibit a flat (0001) growth front surface, all the petal tips were hemispherical. They all showed a very close curvature and radius as well as the dislocation-free crystalline lattices. No wetting layer, catalysts trace or amorphous shell was identified from these petal tips. This unique tip structure indicates that, during the growth, a non-crystalline or liquid state could exist, which turned the faceted top (0001) surface into an isotropic hemispherical shape. Furthermore, the growth directions of these petal tips, as highlighted by the arrows shown in Fig. 2i–k, were not parallel to the [0001] direction. This observation suggests that although the overall petal grew along the [0001] direction, the petal tip tended to shift away from the [0001] direction most likely due to the precursor supply, thus expanded the corolla laterally. The hemispherical tip and the ability to shift the growth direction while maintaining a perfect single-crystalline lattice imply a possible VLS growth process of the petals, where the most possible liquid phase would be the Zn clusters that were condensed from the Zn vapor. EDS study also showed a slightly higher Zn concentration in the ZnO nanoflower region (Fig. S1†).

Growth kinetics analyses

Further analyses were performed to understand why Zn clusters can be precipitated from the vapor phase and then direct the growth of ZnO NWs *via* a self-catalyzed VLS process. First, in our deposition system, ZnO decomposed at high temperature (>1000 °C) into Zn and O_2 gaseous phases. Under this condition, the concentration of ZnO vapor was several orders of magnitude lower than the concentrations of Zn and O_2 vapor.[30–34] Thus, we only considered the interactions between Zn and O_2 when analyzing the kinetics of ZnO nanostructure growth.

In general, the deposition of ZnO from the vapor phase would undergo two possible steps at the temperature region where Zn could sustain as liquid: (1) condensation of Zn from vapor phase to liquid phase: Zn (g) → Zn (l); (2) oxidation of Zn: Zn (l) + $^1/_2$ O_2 (g) → ZnO (s). If the first step was the rate-limiting step, the condensed Zn would immediately be oxidized into ZnO, thus it can be considered as a VS deposition process. If the second step was the rate-limiting step, liquid Zn would accumulate at the surface and a self-catalyzed VLS process would be possible. Based on this rationale, the condensation rate and oxidation rate were both calculated.

The condensation rate is governed by the sticking coefficient (S) and the incident molecular flux (F) *via* the relation $R_{con} = F \times S$. In our calculation, S was simply assumed to be 0.5[35] and F can be estimated by the Hertz–Knudsen equation:[36]

$$F = (P - P_e)/(2\pi mkT)^{1/2} \quad (1)$$

where P is the Zn partial pressure, which can be obtained by the instant decomposition rate of ZnO as a function of temperature, P_e is the equilibrium partial pressure of Zn, m is the mass of Zn atom, and T is the temperature.[30] The equilibrium Zn partial pressure at the tip was estimated based on the value of a flat Zn surface and rectified using the nanosized hemispherical surface geometry (Fig. S2†). The oxidation rate of Zn was estimated using the equation:[30,37]

$$R_{ox} = 5.9 \times 10^8 \exp(-Q/RT)[Zn][O_2]\ \text{mol}^{-1}\ \text{m}^{-3} \quad (2)$$

Considering the oxidation of deposited Zn atoms was a heterogeneous process, the activation energy Q of 128 kJ mol^{-1-1} was utilized.[37] The prefactor was obtained from ref. 27. [Zn] and [O_2] are the concentration of Zn and O_2 vapor concentration in the chamber, respectively. To be noticed, these constant values should be regarded as the first order approximation of our model. The oxidation rate equation was determined based on flat surfaces and is likely to vary in our system due to the irregular morphologies and other growth parameters.[37]

The Zn condensation and oxidation rates were plotted together as a function of the deposition temperature (Fig. 3). The deposition temperature was directly related to the position of the substrate (Fig. S3†). The plot clearly shows that high deposition temperature is favorable for the oxidation of Zn, while at low temperature the Zn condensation would become dominant. These two curves intersect at the temperature of ~680 K, which is near the temperature zone of nanoflower formation. By matching the morphologies obtained at different substrate positions with the two rate curves in Fig. 3, five distinct growth/temperature regions were identified.

At high deposition temperature where the oxidation rate was significantly faster than the condensation rate, ZnO NWs were found to be the dominant morphology (region I in Fig. 3 and Fig. S4†). In this region, the deposition of ZnO was a diffusion-controlled process which has been confirmed by the finite difference mass transfer model in a similar case.[38] The diffusion coefficients of Zn in Ar and O_2 in Ar were estimated to be nearly identical by the Chapman–Enskog equation and numerical simulations.[38,39] The stoichiometric precursor supply and the faster oxidation rate suggest that the formation of ZnO NWs would undergo a VS process. Typical ZnO nanowire growth by vapor deposition falls into this region.[40]

When the substrate temperature moved closer to the intersection point, the ZnO nanocomb structure became dominant (region II in Fig. 3 and Fig. S5†). EDS revealed a similar Zn concentration as that of ZnO nanoflowers. At this region, the nanocomb would still grow *via* a VS process due to the fast oxidation rate. A more rapid and abundant Zn condensation compared to region I would possibly be the reason to choose the formation of the nanocomb structures over straight NWs.

Around the temperature where the condensation and oxidation plots intersect, the nanoflower structure appeared (region III in Fig. 3). In this region, the difference between the condensation and oxidation rates would wobble between small positive and negative values due to local pressure variation. When the Zn condensation rate exceeded the oxidation rate, it became possible for a liquid Zn phase to form and serve as catalysts to direct the growth of ZnO NWs. Based on the perfect wetting property between Zn and ZnO, it is likely that the liquid Zn covered the ZnO NW growth front as a thin layer.[26] This growth phenomenon has been observed in the growth of Cd crystals catalyzed by a wetting layer of Bi film.[41] When the Zn condensation rate dropped lower than the oxidation rate, the liquid Zn would be consumed thus preventing the liquid Zn phase from growing larger. The competition between these two rates could explain the formation of small ZnO nanoflower petals that exhibited hemispherical tips and wavy side surfaces. It should be noted that the region III for the formation of ZnO nanoflowers is rather narrow due to the critical requirement of the reaction kinetics. A transitional region between regions II and III was also identified as a support of this rationale. In that region, bundles of small NWs similar to the nanoflower structure were discovered, whereas, the tips were found to be the flat (0001) surfaces (Fig. S6†). This phenomenon indicates a possible insufficiency of liquid Zn during the growth, which could not completely eliminate the surface energy difference for forming a hemispherical tip.

Further lowering the deposition temperature would result in a rapid condensation of Zn with a rate significantly higher than the rate of oxidation (region IV in Fig. 3). In this region, irregular wire-like nanostructure was observed (Fig. S7a†) and EDS indicates higher Zn concentration (~67%) in this region compared to the nanoflowers (Fig. S7b†). The dark field TEM image (Fig. 3) revealed that these structures were Zn–ZnO core–shell NWs. The epitaxial relationship between the Zn core and ZnO shell was analyzed and confirmed by SAED and HRTEM as shown in Fig. S8†. The formation of Zn–ZnO core–shell NWs was possibly due to the fast condensation rate of Zn followed by a relatively slow surface oxidation. The oxidation of the Zn core

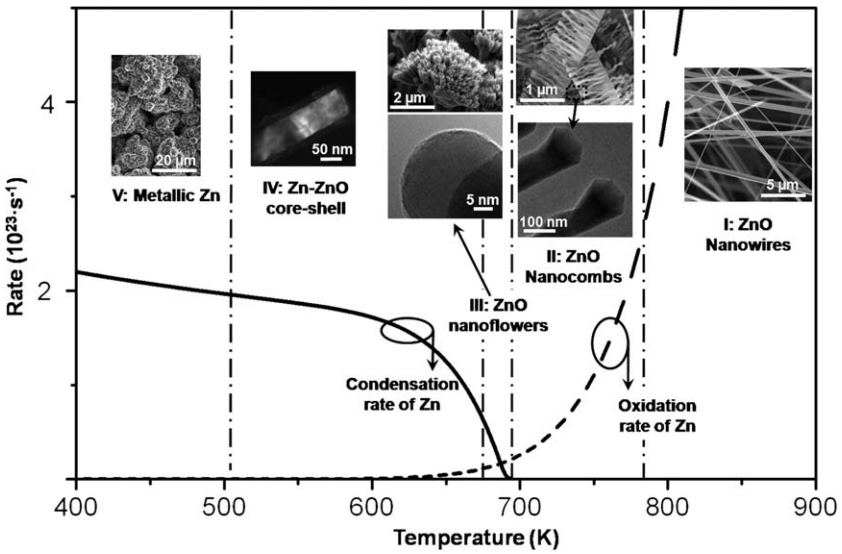

Fig. 3 Plots of oxidation (dashed line) and condensation (solid line) rates of Zn *versus* the substrate temperature. The five distinct deposition regions are marked with dash-dotted lines and illustrated by the inset typical morphology images. Region I: ZnO nanowire is the dominant morphology. Region II: ZnO nanocombs are dominant. Region III: ZnO nanoflowers are dominant. Region IV: Zn–ZnO core–shell structure is dominant. Region V: metallic Zn deposition is dominant.

under ZnO shell is typically controlled by the diffusion of Zn or O_2 through the ZnO surface layer—the Wagner oxidation theory.[42,43]

Below ~500 K is the region V, where the deposition appeared black and was identified as metallic Zn as shown in Fig. 3 and Fig. S9†. The formation of Zn was likely due to the almost negligible Zn oxidation rate compared to the Zn condensation, which is the situation that should be avoided for making any ZnO nanostructures.

Comparison between the deposition and oxidation rates explained the formation of ZnO nanoflower pedals. This kinetic-based theory could also be applied to illustrating the morphology switching from large straight NWs (the stems) to small curvy NWs (the petals). Thermogravimetric experiments have demonstrated that decomposition of ZnO occurs at ~1273 K at atmospheric pressure and in a flow of inert gas.[34] Therefore, Zn and O_2 precursors would become available for growing ZnO nanostructures in the system when the furnace temperature (T_F) reached 1000 °C and above. Noting that the substrate temperature (T_S) is dictated by the T_F (Fig. S2†), the relationship between deposition and oxidation rate would vary under different T_F, which could induce the growth of different morphologies.

Fig. 4a illustrates the deposition/oxidation relationships at four different T_F (1100, 1200, 1300 and 1400 °C) in order to reveal the morphology change during the heating ramp process. The local T_S of the nanoflower growth region is highlighted with grey. When the T_F was ramping up slowly, T_S of the nanoflower region first reached 570 K (Fig. 4a), where the condition was favorable for VS NW growth (T_F = 1100 and 1200 °C) since the oxidation rate of Zn was superior to its condensation rate. Therefore, stems of the nanoflowers would grow at this point (Fig. 4b, stage I). As the T_F increased near the set point (~1400 °C), the T_S of the nanoflower deposition region rose to ~680 K, where the deposition/oxidation relationship is identical to region III in Fig. 3. Under this condition, liquid Zn would appear on the growth front of the big NWs and serve as catalysts to direct the growth of flower petals (stage II in Fig. 4b). Meanwhile, new Zn clusters could be continuously condensed onto the surfaces of the flower petals thereby providing more nucleation sites (stage III of Fig. 4b). Petals then grew off from these nucleation sites and stacked one by one so that the corolla size enlarged (stage IV of Fig. 4b). Eventually, a micrometre-sized corolla formed at the tip of the nanoflower stem (stage V of Fig. 4b). The suggested nucleation on the petal side surfaces and the following epitaxial petal growth are illustrated in the inset of Fig. 4b. This explains why overall nanoflower structure exhibited one identical crystal orientation, although it was composed of thousands of small NW petals. This mechanism was further supported by a control experiment in which the furnace was shut down before it reached 1400 °C, which effectively terminated the formation of corolla. The dominant morphology was tapered NW stems only with sparsely distributed tiny petals (Fig. S9†).

Fluorescence property and applications

The ZnO nanoflowers were observed to show strong green luminescence (GL) at room temperature. Peak wavelength of the fluorescence is at 486 nm. No detectable emission in the visible range was found from the ZnO NWs collected in region I (Fig. 5a). We believe the strong GL was resulted from the non-stoichiometric defects, such as Zn interstitials or oxygen vacancies that were associated with the Zn rich deposition condition.[44] The extremely large surface area and the wavy sidewalls of the petals may also facilitate the recombination of electrons and holes that were trapped at the surface defects, thus contributed to the strong GL property.[45] Owing to the unique stacking configuration, the petals can be broken off by sonication and form a well-dispersed fluorescent suspension in ethanol (Fig. 5b). The potential application for *in vitro* cell labeling was then investigated.

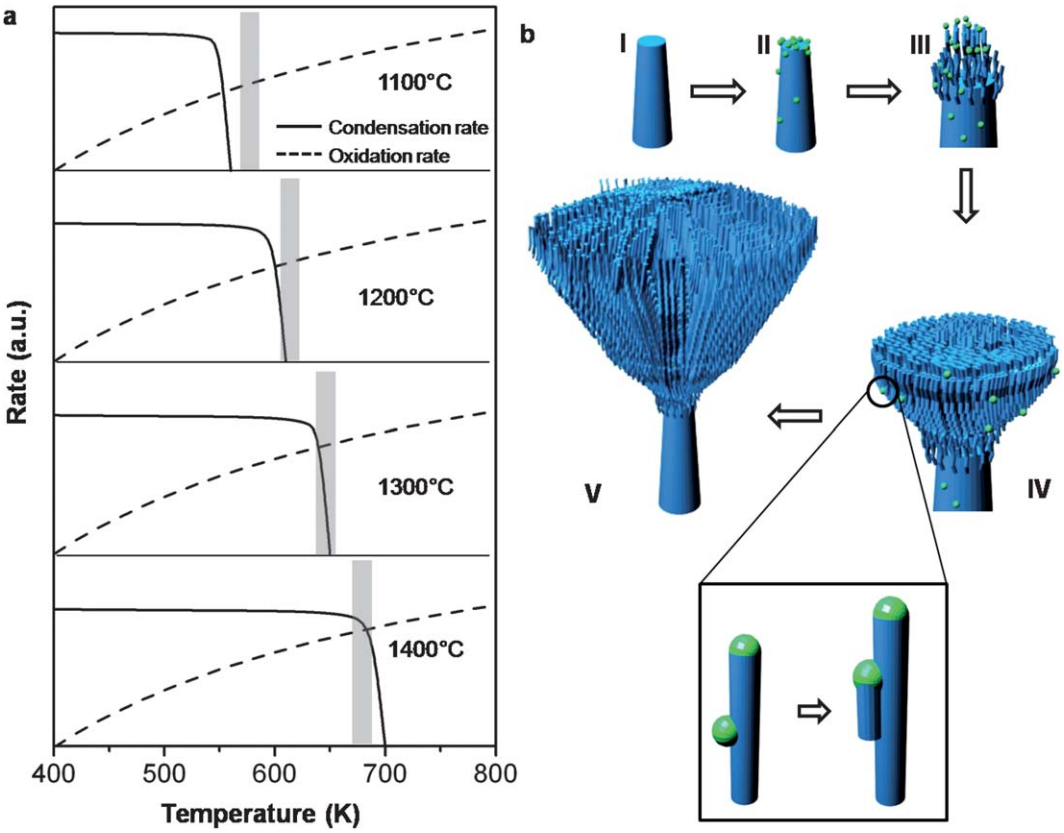

Fig. 4 Growth kinetics and mechanism of nanoflowers. (a) Plots of oxidation and condensation rates of Zn (logarithm values are applied here to magnify the details) *versus* the substrate temperature at different precursor temperatures: 1100 °C, 1200 °C, 1300 °C, and 1400 °C. Grey bars in each subdivision illustrate the temperature ranges of the substrates region where nanoflowers grew. (b) Growth model of nanoflowers. (I) Growth of the stem *via* a vapor–solid process. (II) Formation of Zn clusters by condensation of Zn vapor when the condensation rate is superior to the oxidation rate. (III) Growth of petals catalyzed by Zn clusters and the continuous deposition of Zn clusters by condensation. (IV) Embryonic corolla appears when petals are stacking one over the other. Inset illustrates the Zn-cluster-catalyzed stacking and the epitaxial growth process along the petal's sidewall. (V) Corolla structure was formed by repeating step (IV).

To demonstrate the proof-of-principle that these strongly fluorescent ZnO NWs can be used for optical imaging applications, the small ZnO NWs (the petals) were functionalized with PEG and RGD-containing peptides and investigated in various cancer cells. The RGD peptides are potent antagonists of integrin $\alpha_v\beta_3$, a cell adhesion molecule which plays a key role in tumor angiogenesis and metastasis.[46,47] Expressed on both tumor neovasculature and certain tumor cells, integrin $\alpha_v\beta_3$ is an attractive target for potential nanomaterial-based tumor targeting *in vivo* since extravasation (a major obstacle for most nanomaterials) is not required.[48–50] The U87MG human glioblastoma cell line, which expresses high level of integrin $\alpha_v\beta_3$, was used as a positive control while the MCF-7 human breast cancer cell line (which expresses low level of integrin $\alpha_v\beta_3$) was used as a negative control.[51,52]

As shown in Fig. 5c, the U87MG cells are clearly visualized after incubation with NW–PEG–RGD, but not after incubation with naked NW or NW–PEG. In addition, the fluorescence signal of NW–PEG–RGD can be effectively blocked to background level by 2 μM of c(RGDyK), thus demonstrating the integrin $\alpha_v\beta_3$ specificity of NW–PEG–RGD. Meanwhile, none of the NW conjugates bound to the integrin $\alpha_v\beta_3$-negative MCF-7 cells (Fig. 5d). Minimal fluorescence signal was observed and the fluorescence intensity of naked NW, NW–PEG and NW–PEG–RGD was nearly undistinguishable. Taken together, these cellular studies clearly indicated that NW–PEG–RGD can bind to integrin $\alpha_v\beta_3$ in a receptor-specific manner, with a minimal level of non-specific binding, thus opening up new perspectives for nanomaterial-based optical imaging *in vitro* and potentially *in vivo*.

Conclusion

We studied the ZnO nanostructure growth kinetics under well-controlled experimental conditions. The Zn vapor condensation and oxidation rates were compared and their relationship was used to explain the formation of different ZnO nano-morphologies. The rate analyses revealed a trend of continuous augmentation of composition of the Zn component and the ZnO morphologies as a function of the deposition temperature. The competition between these two rates led to the nanoflower structure—thousands of small curvy NWs bundling on the tip of one large NW. This novel nanostructure evidenced the self-catalyzed growth process of ZnO NWs. It also suggested the possibility of switching the growth mechanism between VS and VLS by controlling the deposition kinetics. The resulting ZnO

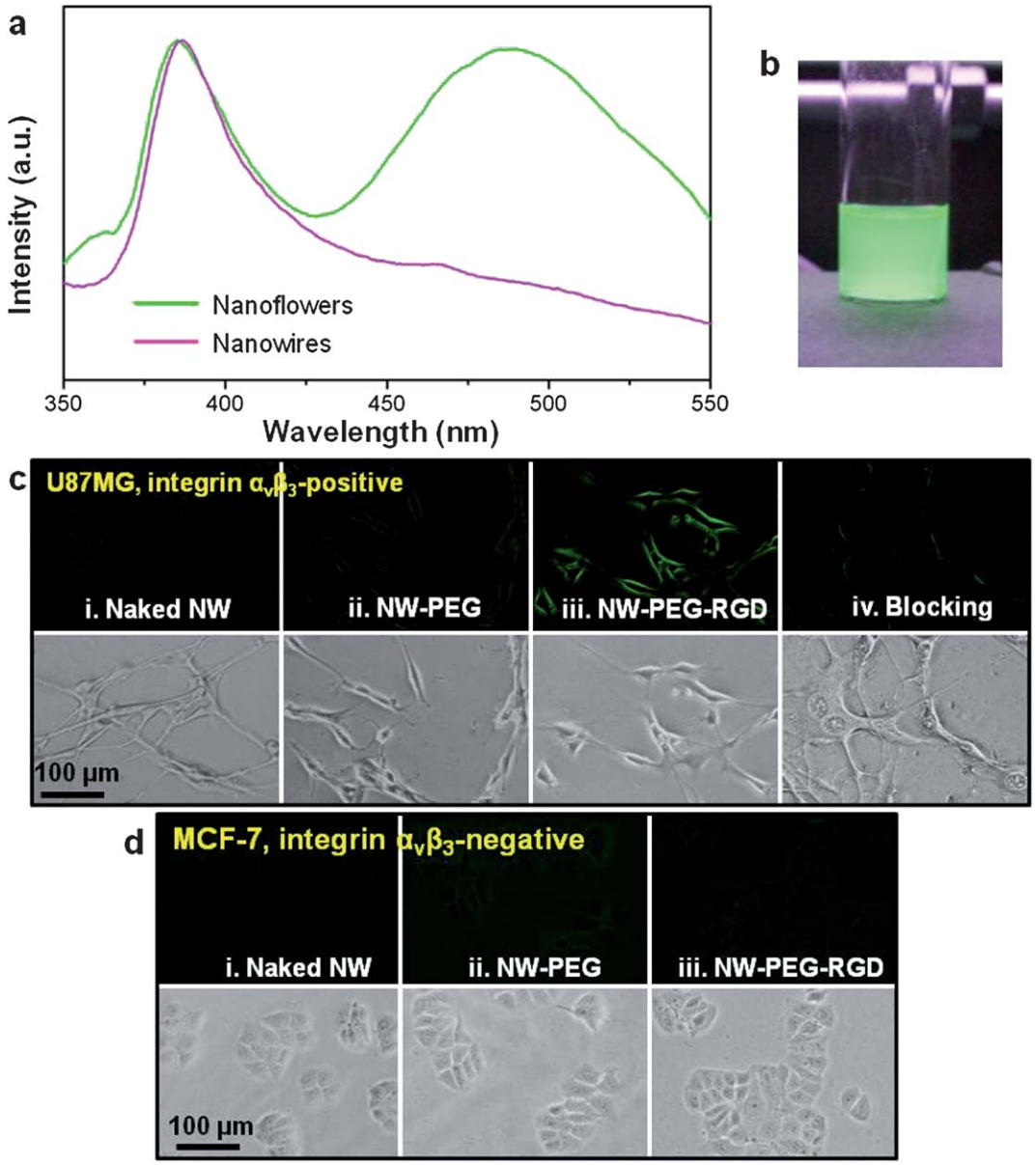

Fig. 5 Cell imaging with the intrinsic green fluorescence of ZnO nanowires. (a) Fluorescence spectra of regular nanowires collected in region I and nanoflowers in region III. Significant green luminescence could be observed from the nanoflowers region, while no notable green luminescence peak could be identified for the nanowires. (b) A bottle of ZnO nanowires that was prepared by breaking nanoflowers into pieces in ultrasonic bath. The solution exhibited a strong green luminescence under a low power UV lamp (4 W). (c) Fluorescent microscopy images of U87MG human glioblastoma cells (high integrin $\alpha_v\beta_3$ expression) after incubation with differently functionalized ZnO nanowires (naked NW: no surface modification; NW–PEG: ZnO nanowires with surface polyethylene glycol conjugation; NW–PEG–RGD: ZnO nanowires with both surface polyethylene glycol and RGD peptide conjugation). Blocking: incubation of fixed U87MG cells with NW–PEG–RGD in the presence of 2 μM of free RGD peptide. (d) Fluorescent microscopy images of differently functionalized ZnO nanowires in MCF-7 human breast cancer cells (low integrin $\alpha_v\beta_3$ expression).

nanoflowers showed strong GL, which were successfully applied for *in vitro* tumor cell imaging. This research discovered a fundamental kinetics that governs the mechanisms and morphology selection of nanostructures in a non-catalyst growth system.

Acknowledgements

J.S. and X.W. thank National Science Foundation under grant No. DMR-0905914. HH, YY and WC thank the support by the UW School of Medicine and Public Health's Medical Education and Research Committee through the Wisconsin Partnership Program, the University of Wisconsin Carbone Cancer Center, a Susan G. Komen Postdoctoral Fellowship, a DOD BCRP Postdoctoral Fellowship and a DOD PCRP IDEA Award.

References

1 S. Barth, F. Hernandez-Ramirez, J. D. Holmes and A. Romano-Rodriguez, *Prog. Mater. Sci.*, 2010, **55**, 563–627.

2 M. Gratzel, *Nature*, 2001, **414**, 338–344.
3 S. V. N. T. Kuchibhatla, A. S. Karakoti, D. Bera and S. Seal, *Prog. Mater. Sci.*, 2007, **52**, 699–913.
4 C. M. Lieber, *Solid State Commun.*, 1998, **107**, 607–616.
5 C. M. Lieber and Z. L. Wang, *MRS Bull.*, 2007, **32**, 99–108.
6 Y. N. Xia, P. D. Yang, Y. G. Sun, Y. Y. Wu, B. Mayers, B. Gates, Y. D. Yin, F. Kim and Y. Q. Yan, *Adv. Mater.*, 2003, **15**, 353–389.
7 R. X. Yan, D. Gargas and P. D. Yang, *Nat. Photonics*, 2009, **3**, 569–576.
8 P. D. Yang, R. X. Yan and M. Fardy, *Nano Lett.*, 2010, **10**, 1529–1536.
9 R. L. Woo, L. Gao, N. Goel, M. K. Hudait, K. L. Wang, S. Kodambaka and R. F. Hicks, *Nano Lett.*, 2009, **9**, 2207–2211.
10 Y. Y. Wu and P. D. Yang, *J. Am. Chem. Soc.*, 2001, **123**, 3165–3166.
11 M. J. Bierman, Y. K. A. Lau, A. V. Kvit, A. L. Schmitt and S. Jin, *Science*, 2008, **320**, 1060–1063.
12 A. D. Gamalski, J. Tersoff, R. Sharma, C. Ducati and S. Hofmann, *Nano Lett.*, 2010, **10**, 2972–2976.
13 J. B. Hannon, S. Kodambaka, F. M. Ross and R. M. Tromp, *Nature*, 2006, **440**, 69–71.
14 B. J. Kim, J. Tersoff, S. Kodambaka, M. C. Reuter, E. A. Stach and F. M. Ross, *Science*, 2008, **322**, 1070–1073.
15 S. Kodambaka, J. Tersoff, M. C. Reuter and F. M. Ross, *Phys. Rev. Lett.*, 2006, **96**, 096105–096105.
16 S. Kodambaka, J. Tersoff, M. C. Reuter and F. M. Ross, *Science*, 2007, **316**, 729–732.
17 F. M. Ross, J. Tersoff and M. C. Reuter, *Phys. Rev. Lett.*, 2005, **95**, 146104–146104.
18 C. Y. Wen, M. C. Reuter, J. Tersoff, E. A. Stach and F. M. Ross, *Nano Lett.*, 2010, **10**, 514–519.
19 C. Y. Wen, J. Tersoff, M. C. Reuter, E. A. Stach and F. M. Ross, *Phys. Rev. Lett.*, 2010, **105**, 195502–195502.
20 B. S. Kim, T. W. Koo, J. H. Lee, D. S. Kim, Y. C. Jung, S. W. Hwang, B. L. Choi, E. K. Lee, J. M. Kim and D. Whang, *Nano Lett.*, 2009, **9**, 864–869.
21 P. Krogstrup, R. Popovitz-Biro, E. Johnson, M. H. Madsen, J. Nygard and H. Shtrikman, *Nano Lett.*, 2010, **10**, 4475–4482.
22 M. Mattila, T. Hakkarainen, H. Lipsanen, H. Jiang and E. I. Kauppinen, *Appl. Phys. Lett.*, 2006, **89**, 063119–063119.
23 Z. W. Pan, Z. R. Dai and Z. L. Wang, *Science*, 2001, **291**, 1947–1949.
24 J. Shi, S. Grutzik and X. D. Wang, *ACS Nano*, 2009, **3**, 1594–1602.
25 E. A. Stach, P. J. Pauzauskie, T. Kuykendall, J. Goldberger, R. R. He and P. D. Yang, *Nano Lett.*, 2003, **3**, 867–869.
26 Z. L. Wang, X. Y. Kong and J. M. Zuo, *Phys. Rev. Lett.*, 2003, **91**, 185502–185502.
27 E. Galoppini, *Coord. Chem. Rev.*, 2004, **248**, 1283–1297.
28 D. Liu, W. Wu, Y. Qiu, S. Yang, S. Xiao, Q. Q. Wang, L. Ding and J. Wang, *Langmuir*, 2008, **24**, 5052–5059.
29 O. Taratula, E. Galoppini, D. Wang, D. Chu, Z. Zhang, H. Chen, G. Saraf and Y. Lu, *J. Phys. Chem. B*, 2006, **110**, 6506–6515.
30 R. Palumbo, J. Lede, O. Boutin, E. E. Ricart, A. Steinfeld, S. Moller, A. Weidenkaff, E. A. Fletcher and J. Bielicki, *Chem. Eng. Sci.*, 1998, **53**, 2503–2517.
31 S. Abanades, P. Charvin and G. Flamant, *Chem. Eng. Sci.*, 2007, **62**, 6323–6333.
32 P. Haueter, S. Moeller, R. Palumbo and A. Steinfeld, *Sol. Energy*, 1999, **67**, 161–167.
33 S. Moller and R. Palumbo, *Chem. Eng. Sci.*, 2001, **56**, 4505–4515.
34 A. Weidenkaff, A. Steinfeld, A. Wokaun, P. O. Auer, B. Eichler and A. Reller, *Sol. Energy*, 1999, **65**, 59–69.
35 W. Mokwa, D. Kohl and G. Heiland, *Surf. Sci.*, 1980, **99**, 202–212.
36 A. Rockett, *The Materials Science of Semiconductors*, Springer, New York, 2008.
37 H. Delalu, J. R. Vignalou, M. Elkhatib and R. Metz, *Solid State Sci.*, 2000, **2**, 229–235.
38 M. Keunecke, A. Meier and R. Palumbo, *Chem. Eng. Sci.*, 2004, **59**, 2695–2704.
39 A. B. Murphy, *Plasma Chem. Plasma Process.*, 1995, **15**, 279–307.
40 Z. L. Wang, *J. Phys.: Condens. Matter*, 2004, **16**, R829–R858.
41 R. R. Hasiguti, H. Yumoto and Y. Kuriyama, *J. Cryst. Growth*, 1981, **52**, 135–140.
42 X. Y. Kong, Y. Ding and Z. L. Wang, *J. Phys. Chem. B*, 2004, **108**, 570–574.
43 A. Weidenkaff, A. Reller, F. Sibieude, A. Wokaun and A. Steinfeld, *Chem. Mater.*, 2000, **12**, 2175–2181.
44 N. E. Hsu, W. K. Hung and Y. F. Chen, *J. Appl. Phys.*, 2004, **96**, 4671–4673.
45 M. Foley, C. Ton-That and M. R. Phillips, *Appl. Phys. Lett.*, 2008, **93**, 243104–243104.
46 W. Cai, G. Niu and X. Chen, *Curr. Pharm. Des.*, 2008, **14**, 2943–2973.
47 J. P. Xiong, T. Stehle, R. Zhang, A. Joachimiak, M. Frech, S. L. Goodman and M. A. Arnaout, *Science*, 2002, **296**, 151–155.
48 W. Cai, K. Chen, Z. B. Li, S. S. Gambhir and X. Chen, *J. Nucl. Med.*, 2007, **48**, 1862–1870.
49 W. Cai and X. Chen, *Small*, 2007, **3**, 1840–1854.
50 W. Cai and X. Chen, *J. Nucl. Med.*, 2008, **49**(suppl. 2), 113S–128S.
51 W. Cai, D. W. Shin, K. Chen, O. Gheysens, Q. Cao, S. X. Wang, S. S. Gambhir and X. Chen, *Nano Lett.*, 2006, **6**, 669–676.
52 Z. Liu, W. Cai, L. He, N. Nakayama, K. Chen, X. Sun, X. Chen and H. Dai, *Nat. Nanotechnol.*, 2006, **2**, 47–52.